Progress in Reaction Kinetics and Mechanism, 2018, 43(3–4), 201–210
https://doi.org/10.3184/146867818X15233705894419 Paper: 1700647

Mechanism of nanostructured fluorapatite formation from CaO, CaF_2 and P_2O_5 precursors by mechanochemical synthesis

Raheleh Nikonam Mofrad[a]*, Sayed Khatiboleslam Sadrnezhaad[b] and Jalil Vahdati Khaki[c]

[a]*Department of Mechanical, Industrial and Aerospace Engineering, Concordia University, 1455 De Maisonneuve Blvd. W., Montreal, Quebec, Canada H3G 1M8*

[b]*Department of Materials Science and Engineering, Sharif University of Technology, PO Box 11365-9466, Tehran, Iran*

[c]*Department of Material Engineering, Faculty of Engineering, Ferdowsi University of Mashhad, PO Box 91775-1111, Mashhad, Iran*

**E-mail: rahele_nikonam@ymail.com*

ABSTRACT

We determined the mechanism of mechanochemical synthesis of fluorapatite from CaO, CaF_2 and P_2O_5 by characterisation of the intermediate compounds. We used atomic absorption spectroscopy, X-ray diffraction, field emission scanning electron microscopy, FTIR spectroscopy and transmission electron microscopy to find the transitional compounds. Investigation of the binary and ternary powder mixtures revealed the appearance of H_3PO_4, $Ca(OH)_2$, $Ca_2P_2O_7$ and $CaCO_3$ as the intermediate compounds. At early stages of the milling, conversions of P_2O_5 to H_3PO_4 and CaO to $Ca(OH)_2$ occurred in the wet atmosphere. Later, a combination of $Ca(OH)_2$ and H_3PO_4 formed $Ca_2P_2O_7$ while the unreacted CaO was converted to $CaCO_3$ by CO_2 of the ambient atmosphere. Spherical crystalline $Ca_{10}(PO_4)_6F_2$ particles formed after 48 hours of milling due to the reaction between $Ca_2P_2O_7$, $CaCO_3$ and CaF_2.

KEYWORDS: mechanochemical process, nanostructured fluorapatite, reaction mechanism, intermediate compounds

1. INTRODUCTION

Statistics show that around 8.9 million fractures happen annually due to osteoporosis which targets about one in three women and one in five men over age 50 [1]. Designing new calcium phosphate (CP)-based implants and substitutes for regeneration and repair of bone and teeth defects has therefore grown considerably in recent years [2–4]. The well-known biocompatible CP, fluorapatite (FA) [$Ca_{10}(PO_4)_6F_2$] has found wide applications for clinical use [5]. Studies have shown that FA has better thermal and chemical stability in simulated body fluid than hydroxyapatite [6–8].

The presence of fluorine in the culture medium results in dental and skeletal development and prevention of dental caries formation [9]. It stimulates osteoblastic and alkaline phosphatase activities in terms of cell proliferation and differentiation [10,11]. According to the literature [12], these properties are enhanced when the polycrystalline solids are of nanometric size with grains of less than 100 nm diameter. The unique properties of these materials arise from their high surface-to-volume ratio and large number of atoms residing near their grain boundaries [13].

Mechanochemical synthesis is a simple method for preparation of nanostructured materials in both experimental and commercial quantities [14]. Although diverse techniques can be used to produce FA powder [15–21], mechanochemical synthesis seems to be a more reliable and effective method [22–24]. The intensive mechanical collisions that take place during the high-energy ball milling of the constituent materials result in initiation of solid-state reactions which end up with FA formation. Considering that the purity of the final products and the efficiency of the utilised synthesis processes depend highly on the formation reactions, recently many investigations have concentrated on the FA formation mechanism [23,25,26]. To find out the reaction pathways and the intermediate species that participate in the overall formation reaction, comprehensive understanding of the details of the governing steps is required.

We aimed to find the intermediate steps which lead to the formation of the nanocrystalline $Ca_{10}(PO_4)_6F_2$ by the mechanochemical method. While most FA is produced using calcium carbonate ($CaCO_3$) or calcium hydroxide [$Ca(OH)_2$] as a source of calcium [23,25,26], in this research the formation mechanism and intermediate compounds were studied using calcium oxide (CaO), calcium fluoride (CaF_2) and phosphorus oxide (P_2O_5) as the starting materials. For monitoring the progress of the reactions, we used X-ray diffraction (XRD) analysis to characterise the intermediate compounds. In order to determine the reactivity of the reactants and the sequences of formation of the intermediate compounds, we investigated three binary and four ternary milling routes ending up with the FA nanostructure. The data obtained were more detailed than information given by previous authors [23–27] and could assist us to propose a more comprehensive explanation for the FA formation process.

2. MATERIALS AND METHODS

We used CaO (BDH, catalogue no. 11021-462, min. 95% purity), P_2O_5 (BDH, catalogue no. 21411, min. 98.5% purity) and CaF_2 (MERCK, product no. 102840, precipitated pure with mean particle size of about 100 μm) as the source of calcium, phosphorus, fluoride and oxygen with a $CaO:P_2O_5:CaF_2$ molar ratio of 9:3:1 based on the stoichiometric ratio of the following reaction to prepare FA powder

$$9CaO(s) + 3P_2O_5(s) + CaF_2(s) \rightarrow Ca_{10}(PO_4)_6F_2(s) \quad (1)$$

where 's' represents the solid state.

We charged the mixture into a stainless steel vial containing stainless steel balls of 1 cm diameter. The ball-to-precursor weight ratio was 40:1. The milling rotational speed was 260 rpm in accordance with a pre-specified schedule. We performed two sets of milling regimes to define the formation mechanism of FA powder. First, we milled three binary $CaO–CaF_2$, $P_2O_5–CaF_2$ and $CaO–P_2O_5$ mixtures. These were labelled CFy, PFy and CPy, where y represented the milling time.

In three of the four ternary milling sets, first, two precursors were mechanically activated for 3 h to accelerate the final reaction. Then, the remaining third reactant was added to the system followed by a milling step of up to 48 h. The resulting powders were labelled as CF3Py, PF3Cy and CP3Fy where y represented the milling time. The fourth ternary system consisted of all three reactants which were charged into the vial and milled for different times up to 48 h. The product of this process was named CPFy. The detailed sequences are illustrated in Figure 1.

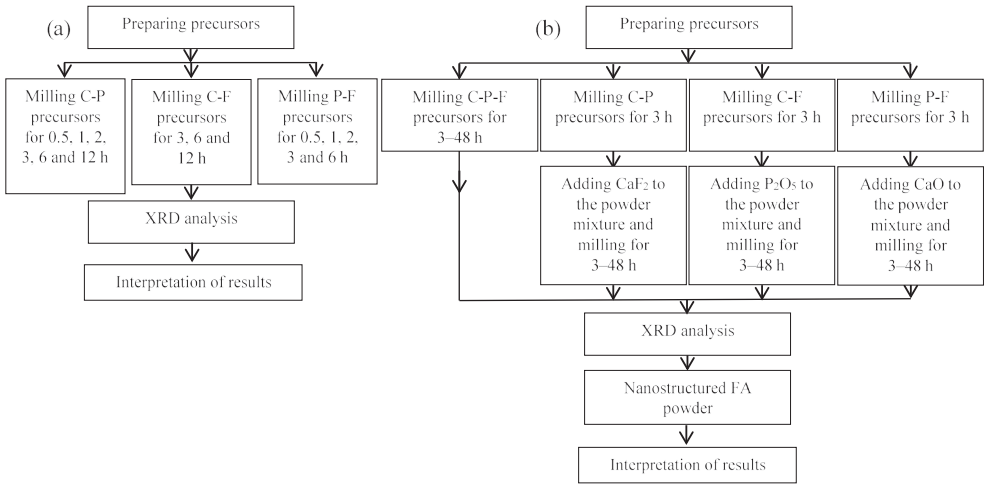

Figure 1 Flowchart of (a) binary and (b) ternary milling systems.

XRD spectra of the samples were obtained on a Philips Analytical X-Ray B.V. diffractometer using Ni-filtered Cu Kα radiation from 2θ = 10 to 60° with a step size of 0.02°, a generating voltage of 40 kV and an electric current of 40 mA. JCPDS standard cards; No: # 02-1088 for CaO, # 35-0816 for CaF_2, # 85-1120 for P_2O_5, # 81-2040 for $Ca(OH)_2$, # 85-0846 for $CaCO_3$, # 83-0688 for phosphoric acid (H_3PO_4), # 03-0604 for calcium phosphate ($Ca_2P_2O_7$) and # 15-0876 for FA were used to define the phase characterisation of the prepared samples. The average crystallite sizes of the products were estimated from peak broadening of the XRD patterns based on the Williamson–Hall (W–H) formula.

$$\beta \cos(\theta) = 0.9\lambda/d + 4\varepsilon \sin(\theta) \quad (2)$$

where d is the average crystallite size (nm), λ is the X-ray wavelength (λ = 0.1540 nm for Cu Kα radiation), β is the broadening of the diffraction peak measured at half peak intensity (in radians), θ is the Bragg diffraction angle (°) and ε is the lattice strain. The full-width at half-maximum (FWHM) of the 002, 213 and 222 reflections (which were sharper and isolated from the others) were taken to measure the crystallite sizes of the FA powder.

The a and c apatite lattice parameters were measured with the XRD data of the (002) and the (222) planes and using the standard formula for the hexagonal close packed system according to Eqn (3) [29]

$$d = [(4/3a^2)(h^2 + hk + k^2) + (l^2/c^2)]^{-1/2} \quad (3)$$

where d is the spacing between the adjacent planes in the Miller indices set (hkl).

Atomic absorption spectroscopy (AAS, GBC, Avanta) of the samples gave the iron concentration of the synthetic powders due to the vial wear during the milling operation. FTIR spectroscopy was performed using an ABB Bomen model MB 100 instrument to collect the spectral data of the samples in the spectral range 400–4000 cm^{-1} with resolution of 4 cm^{-1} by using the KBr pellet technique.

A transmission electron microscope (TEM, LEO 912 AB, Germany) operating at an accelerating voltage of 120 kV was employed to observe the morphology and the particle size of the FA

powder. Morphological investigations were also conducted by field emission scanning electron microscopy (FESEM, Hitachi, S-4160, Japan) of the samples at an acceleration voltage of 15 kV.

3. RESULTS AND DISCUSSION

3.1 X-ray diffraction evaluations

Figure 2(a) plots the XRD patterns of the CPy powder mixture for y = 0.5, 1, 2, 3 and 6 h. As is seen in the figure, after 0.5 h milling, sharp peaks corresponding to $Ca(OH)_2$, $Ca_2P_2O_7$ and H_3PO_4 are present in the mixture. This indicates that due to their high hydrophilicity, P_2O_5 and CaO absorb ambient moisture and form H_3PO_4 and $Ca(OH)_2$ at the early stages of the milling operation through Eqns (4) and (5) respectively.

During the first 30 min of the milling process, $Ca_2P_2O_7$ was formed by a reaction between $Ca(OH)_2$ and H_3PO_4 [Eqn (6)], which shows the high reactivity of these two compounds. After 1 h of milling, the peaks associated with $Ca(OH)_2$ and H_3PO_4 completely vanished and the only remaining compound was $Ca_2P_2O_7$. In the case of CF3, due to the prolonged milling time, the grain size decreased and the volume-fraction of the grain-boundaries increased and eventually the powder mixture mainly consisted of amorphous phases.

$$P_2O_5 + 3H_2O \rightarrow 2H_3PO_4 \qquad \Delta G^\circ_{298K} = -174.19 \text{ kJ mol}^{-1} \quad \Delta H^\circ_{298K} = -181.23 \text{ kJ mol}^{-1} \qquad (4)$$

$$CaO + H_2O \rightarrow Ca(OH)_2 \qquad \Delta G^\circ_{298K} = -57.69 \text{ kJ mol}^{-1} \quad \Delta H^\circ_{298K} = -64.37 \text{ kJ mol}^{-1} \qquad (5)$$

$$2H_3PO_4 + 2Ca(OH)_2 \rightarrow Ca_2P_2O_7 + 5H_2O \qquad \Delta G^\circ_{298K} = -297.83 \text{ kJ mol}^{-1} \quad \Delta H^\circ_{298K} = -288.69 \text{ kJ mol}^{-1} \qquad (6)$$

The XRD patterns of the CFy powder mixtures milled for y = 3, 6 and 12 h are shown in Figure 2(b). In the pattern of CF3, in addition to the peaks attributed to CaF_2, sharp peaks of $Ca(OH)_2$ were also detected which showed the early transformation of CaO into $Ca(OH)_2$. The XRD patterns also reveal the presence of crystalline $CaCO_3$ in the powder mixture even after 12 h of milling. Based on the JCPDS standard card, the first peak of $CaCO_3$ at $2\theta = 29°$ presents in the CF3 XRD pattern. The second and third peaks, which are relatively weak, could overlap with CaF_2 and $Ca(OH)_2$ peaks at $2\theta = 47°$. Although the milling process is done in a sealed vial, it seems that the mechanically-activated CaO becomes reactive to capture CO_2 during the milling process. Considering that the purity of the starting CaO and CaF_2 is high, this impurity comes from the ambient atmosphere. While the initial powder mixture contains CaO with a ratio of 3:1 over P_2O_5, the unreacted CaO could be transformed to $CaCO_3$ under the CO_2-containing atmosphere by the following equation

$$CaO + CO_2 \rightarrow CaCO_3 \quad \Delta G^\circ_{298K} = -130.92 \text{ kJ mol}^{-1} \quad \Delta H^\circ_{298K} = -178.28 \text{ kJ mol}^{-1} \qquad (7)$$

On increasing the milling time to 12 h, no noticeable changes occurred in the XRD pattern, except some broadening and decreasing in the intensity of the $CaCO_3$ peak. This implies that the powder particle size became smaller without formation of a new phase. No reaction occurred between CaO and CaF_2 during this 12 h of milling.

XRD patterns of the PFy powder mixtures milled for y = 0.5, 1, 2, 3 and 6 h are indicated in Figure 2(c). In the PF0.5 spectrum, characteristic peaks of both CaF_2 and P_2O_5 are clearly observable. Despite the high hydrophilicity of P_2O_5, H_3PO_4 is not present in this sample which could be due to the low level of humidity of the ambient air during the experiment. When the mechanical activation time was extended to 2 h, all peaks corresponding to P_2O_5 vanished,

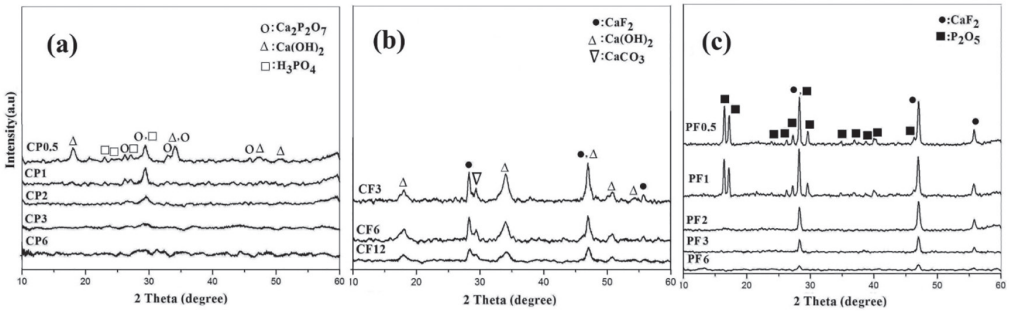

Figure 2 XRD diffractograms of the mechanically treated mixtures of (a) CPy, (b) CFy and (c) PFy binary mixtures, where numbers refer to milling time in h.

but CaF_2 peaks were still visible. After milling for 6 h, no crystalline phases forming due to a reaction between CaF_2 and P_2O_5 were detected.

In these binary systems, while after 3 h no crystalline phases present in the CP system, for PF a fully amorphous pattern is observed after 6 h of milling; however, in the CF system, even after 12 h of milling clear signs of crystalline CaF_2 and $Ca(OH)_2$ were found in the XRD pattern.

Figure 3(a) shows the XRD patterns of the CP3Fy powder mixture milled for y = 3, 6, 12, 24 and 48 h. In the case of the CP3F3 powder, sharp CaF_2 peaks are observable, while no traces of CaO or P_2O_5 are detected. This agrees well with the XRD pattern of the CP3 system which is shown in Figure 2(a) where any peaks corresponding to CaO and P_2O_5 phases vanish after 3 h milling. The broad weak peaks appearing at $2\theta = 25.95$ and 32.14° indicate the formation of the apatite phase after 24 h milling. However, the presence of CaF_2 peaks in these patterns indicates that the formation process is not yet complete. As the milling time exceeds 24 h, further increase in the crystalline order of the apatite phase and further sharpening of the principal diffraction peaks occur. Since the XRD pattern of the CP3F48 is in good agreement with that of the standard FA crystals and no other phases are detectable after 48 h milling, it is concluded that almost the entire amount of the initial powder mixtures react to form the relatively well-crystalline FA sample using this milling route.

Plots of the XRD spectra of the CF3Py powder mixtures milled for y = 3, 6, 12, 28 and 48 h are shown in Figure 3(b). While no peaks of CaO and P_2O_5 are seen in these patterns, $Ca_2P_2O_7$ peaks appear after 3 h milling. Sharp characteristic peaks of CaF_2 are detectable in the 3, 6, 12 and 24 h milled samples. After 24 h of milling, the characteristic peaks of CaF_2 are weakened and broadened while those peaks corresponding to the poorly crystalline FA gradually form. After milling for 48 h, the XRD pattern of the prepared FA becomes strong and sharp. This confirms the formation of the relatively well-crystalline FA phase.

Figure 3(c) shows the XRD pattern of the PF3Cy mixture milled for y = 3, 6, 12 and 48 h. By adding CaO to the PF3 powder mixture and milling for 3 h, in the case where no moisture absorption occurs CaO reacts with P_2O_5 to form $Ca_2P_2O_7$. After milling for 12 h, while CaF_2 peaks are still visible in the XRD pattern, the appearance of some new peaks implies the formation of a poorly crystalline apatite phase. With increase of the milling time up to 48 h, an increase in the XRD intensity of the apatite peaks indicates formation of well-crystalline FA.

The XRD patterns of the CPFy mixture milled for y = 3, 6, 12 and 48 h are shown in Figure 3(d). After milling for 3, 6 and 12 h, the only crystalline phase is CaF_2. The CPF12 sample indicates the presence of a few broad peaks around $2\theta = 31.75$ and 25.83° which seems to be

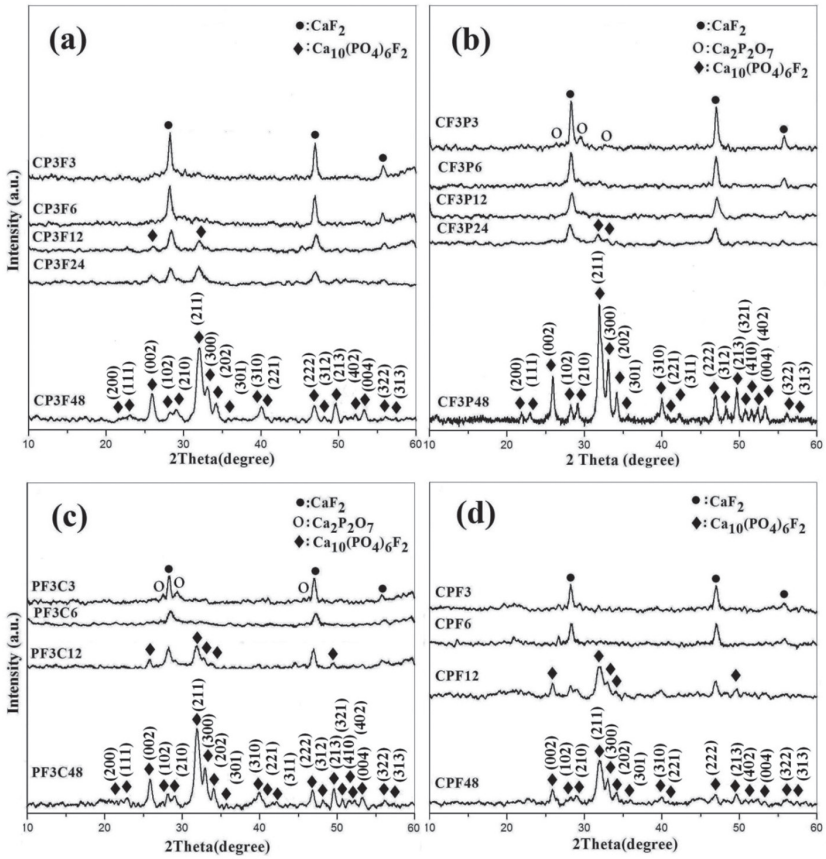

Figure 3 XRD diffractograms of the mechanochemically treated mixtures of (a) CP3Fy, (b) CF3Py, (c) PF3Cy and (d) CPFy ternary systems, where numbers refer to milling time in h.

the fingerprint of the apatite phase. The broad envelope-shaped peaks reveal that the newly formed apatite is poorly crystalline. As the milling time reaches 48 h, the only detectable peaks correspond to FA. This reveals the progression of the well-crystalline FA formation.

While formation of FA appears in the CF3Py system only after 24 h of milling, in the other three systems clear signs of crystalline FA are observed after 12 h of milling. However, after 48 h of milling, CF3P48 shows the highest peak intensity and sharpness which implies the strong crystallinity of this product. This could be due to the relatively longer milling process on CaF_2-containing samples which mechanically activates CaF_2 to react with the other compounds to make a well-crystalline FA powder. PF3C48 also shows higher peak intensities than CP3F48 and CPF48 which confirms the role of CaF_2 mechanical activation on the peak intensities of the FA powder.

Table 1 summarises the lattice parameters of the produced powders which demonstrates that the obtained synthetic FA samples have essentially the same lattice parameters as those based on the JCPDS standard file.

From the XRD observations, it is suggested that the synthesis of FA using CaO, CaF_2 and P_2O_5 proceeds in several stages by forming intermediate products. Detection of the intermediate $Ca(OH)_2$, H_3PO_4, $Ca_2P_2O_7$ and $CaCO_3$ compounds by the XRD patterns confirms the validity

Table 1 Lattice parameters of FA powders produced by different routes

Sample	*a* (nm)	*c* (nm)
FA # 15-0876	0.9368	0.6884
CPF48	0.9358	0.6862
CP3F48	0.9370	0.6876
PF3C48	0.9386	0.6888
CF3P48	0.9385	0.6870

of the sequential formation mechanism. While the above-mentioned phases were formed during the early stages of milling, CaF_2 was the last precursor to participate in the formation reaction. It seems that this phase did not directly react with either CaO or P_2O_5. Formation of fully crystalline $Ca_{10}(PO_4)_6F_2$ eventually occurs due to the reaction between $Ca_2P_2O_7$, CaF_2 and $CaCO_3$ after 48 h of milling as shown in Eqn (8).

$$3Ca_2P_2O_7 + 3CaCO_3 + CaF_2 \rightarrow Ca_{10}(PO_4)_6F_2 + 3CO_2\,(g) \quad (8)$$

$$\Delta G^{\circ}_{298K} = -143.93 \text{ kJ mol}^{-1} \qquad \Delta H^{\circ}_{298K} = +96.89 \text{ kJ mol}^{-1}$$

During the milling process, CO_2 gas may be released to the atmosphere. However, the FTIR analysis reveals a slight fingerprint of CO_3^{2-} group substitution in the PO_4^{3-} sites of the apatite lattice, which is discussed in Section 3.2.

In this research, no trace of any other calcium phosphate phases, *e.g.* $CaHPO_4$ and $Ca_3(PO_4)_2$ was detected in the XRD patterns of the mechanochemically-treated mixtures. This indicates that the amount of impurities in the produced apatite is negligible. AAS analysis shows that the iron concentration of the final powder (sample CF3P48) is 0.51 wt%, which is less than the detection limit of the XRD measurement. This confirms the capability of the mechanochemical route to produce relatively pure FA powder.

3.2 FTIR analysis

Figure 4 presents the FTIR spectrum of the FA nanocrystals prepared after 48 h of milling of the CF3P48. The peak at 471 cm^{-1} corresponds to the asymmetrical υ_2 stretching vibration of PO_4^{3-} [23,24]. The υ_4 bending vibration of this group appears as two peaks at 568 and 599 cm^{-1} [22,30]. The band at 743 cm^{-1} is due to the increase of F^- content in the (OH^-, F^-) chain of apatite. When almost pure FA is obtained, OH···F is predominant in the F^- rich chains containing only a few OH^- groups [31]. The υ_1 bending vibration of the phosphate group appears at 964 cm^{-1} [22] and the most intense bands in the spectrum relating to the asymmetrical υ_3 stretching vibration of the phosphate group appear at 1050 and 1093 cm^{-1} [22,23].

The band at 874 cm^{-1} and a weak band at 1460 cm^{-1} correspond to the υ_2 and υ_3 stretching vibrations of the carbonate groups which shows substitution of CO_3^{2-} groups in PO_4^{3-} sites of the apatite lattice (B-type substitution). Since carbonate groups are a part of hard tissue structures, this low content of CO_3^{2-} groups could improve the bioactivity of FA and makes it more similar to biological components [32,33]. The sharp band at 1645 cm^{-1} and the broad band over 3800–2500 cm^{-1} are attributed to the vibrations of the hydroxyl group originating from the absorbed water in the sample and/or in the KBr pellet [23,24].

3.3 Microscopic analysis

The FESEM micrographs in Figure 5 show the particle size distribution and morphology of the FA powder prepared through mechanochemical synthesis by the CF3P48 route. It can be

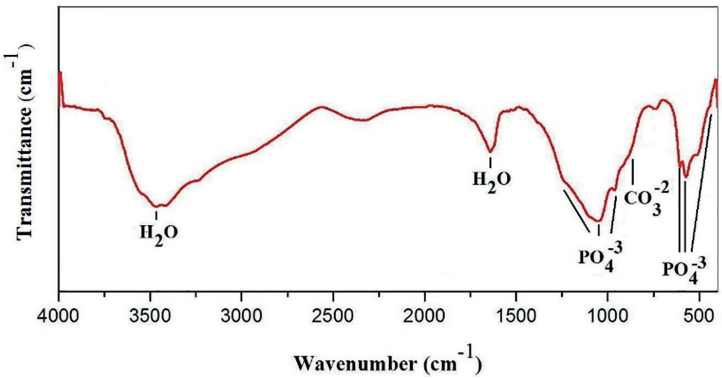

Figure 4 FTIR spectrum of the resulting FA nanocrystals.

noted that the nanoscale particles tend to make agglomerates with irregular shapes and wide size distribution. Higher magnification shows the surface of the agglomerates which are made up of small particles. TEM micrographs of the FA particles (CF3P48) in Figure 6 show that the agglomerates consist of nano-sized semicircular crystals with an average size of 20–40 nm which is in good agreement with the average crystallite size (~34 nm) determined by the W–H formula.

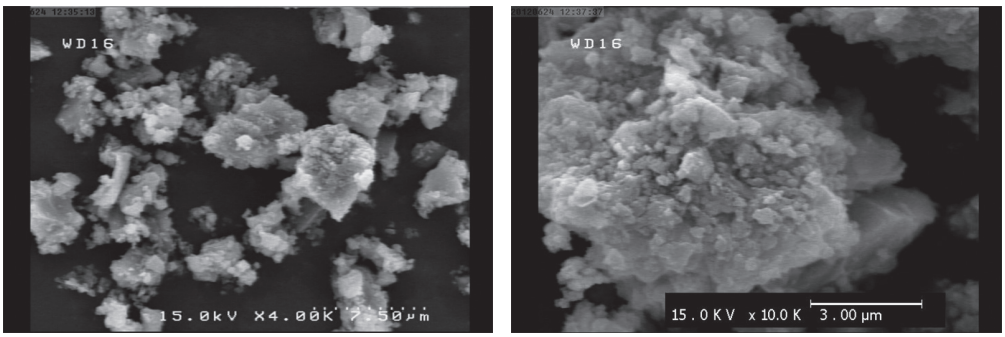

Figure 5 FESEM micrographs of FA particle morphologies.

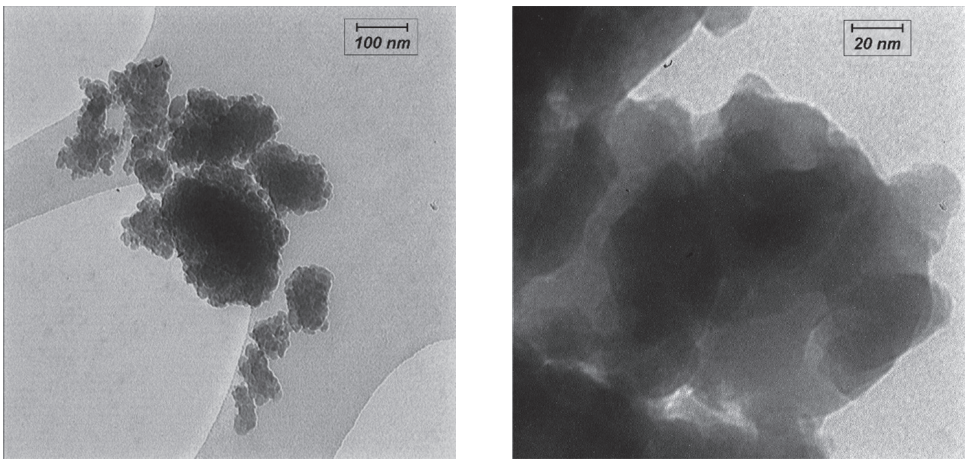

Figure 6 TEM images of FA particle morphologies.

4. CONCLUSIONS

In this study, we have investigated the synthesis and characterisation of FA powder from the starting materials of CaO, CaF_2 and P_2O_5 through a mechanochemical route. The formation mechanism of FA powder was monitored using XRD and FTIR analysis. The results obtained are summarised as follows:

(1) XRD and FTIR analyses showed that a set of solid state reactions ended up with the formation of well-crystalline FA when the precursors were milled together.

(2) The FA formation comprises several intermediate stages. In a humid atmosphere, P_2O_5 absorbed water to form H_3PO_4 and CaO converted to $Ca(OH)_2$. $CaCO_3$ was formed when CaO captured CO_2 of the ambient atmosphere. Reaction of H_3PO_4 and $Ca(OH)_2$ led to the formation of $Ca_2P_2O_7$. CaF_2 was the last precursor which reacted with $Ca_2P_2O_7$ and $CaCO_3$ to eventually form crystalline FA powder after 48 h of milling. Since no reaction directly occurred between CaF_2 and CaO or P_2O_3, a pre-milling step of CaF_2 could help to get a well-crystalline FA powder.

(3) The broadness of the XRD peaks of the final FA indicated that the size of the produced powder was in the nanometre scale which was confirmed by both the TEM examination and the crystallite size measurement of the FA particles using the W–H formula (~34 nm).

(4) The final product had a spherical shape with a tendency to form agglomerates during the milling process.

5. ACKNOWLEDGEMENTS

We thank Sharif University of Technology, the Iran National Science Foundation and the Iran Nanotechnology Initiative Council for their support of our research activities.

Published online: 10 October 2018

6. REFERENCES

[1] https://www.iofbonehealth.org/facts-statistics, International Osteoporosis Foundation. [accessed 23 June 2018].
[2] Dorozhkin, S.V. (2007) *Glass Ceram.,* **64**, 26–31.
[3] Xie, C., Lu, H., Li, W. *et al.* (2012) *J. Mater. Sci.: Mater. Med.,* **23**, 853–862.
[4] Kumta, P.N., Sfeir, C., Lee, D.-H. *et al.* (2005) *Acta Biomater.,* **1**, 65–83.
[5] Wang, H., Sun, K., Li, A. *et al.* (2011) *Powder Technol.,* **209**, 9–14.
[6] Rodriguez-Lorenzo, L.M., Hart, J.N. and Gross, K.A. (2003) *Biomaterials,* **24**, 3777–3785.
[7] Leroy, N. and Bres, E. (2001) *Eur. Cells Mater.,* **2**, 36–48.
[8] Chen, Y. and Miao, X. (2005) *Biomaterials,* **26**, 1205–1210.
[9] Wang, Y., Zhang, S., Zeng, X. *et al.* (2008) *J. Biomed. Mater. Res., Part A,* **84**, 769–776.
[10] Qu, H. and Wei, M. (2006) *Acta Biomater.,* **2**, 113–119.
[11] Yao, F., LeGeros, J.P. and LeGeros, R.Z. (2009) *Acta Biomater.,* **5**, 2169–2177.
[12] Shi, Z., Huang, X., Cai, Y. *et al.* (2009) *Acta Biomater.,* **5**, 338–345.
[13] Suryanarayana, C. (2002) *JOM,* **54**, 24–27.
[14] Suryanarayana, C. (2001) *Prog. Mater. Sci.,* **46**, 1–184.
[15] Qu, H. and Wei, M. (2005) *J. Mater. Sci.: Mater. Med.,* **16**, 129–133.
[16] Cheng, K., Zhang, S. and Weng, W. (2006) *J. Sol-Gel. Sci. Technol.,* **38**, 13–17.
[17] Tredwin, C.J., Young, A.M., Georgiou, G. *et al.* (2012) *Dent. Mater.,* **29**, 166–173.
[18] Chen, H., Sun, K., Tang, Z.*et al.* (2006) *Cryst. Growth Des.,* **6**, 1504–1508.
[19] Zhang, H.G., Zhu, Q. and Xie, Z.H. (2005) *Mater. Res. Bull.,* **40**, 1326–1334.
[20] Wei, M., Evans, J.H., Bostrom, T. and Grøndahl, L (2003) *J. Mater. Sci.: Mater. Med.,* **14**, 311–320.
[21] Partenfelder, U., Engel, A. and Rüssel, C. (1993) *J. Mater. Sci.: Mater. Med.,* **4**, 292–295.
[22] Nasiri-Tabrizi, B. and Fahami A. (2013) *Ceram. Int.,* **39**, 4329–4337.
[23] Fereshteh, Z., Fathi, M. and Mozaffarinia, R. (2015) *J. Clust. Sci.,* **26**, 1041–1053.
[24] Nikčević, I., Jokanović, V., Mitrić, M. *et al.* (2004) *J. Solid State Chem.,* **177**, 2565–2574.

[25] Jokanović, V., Čolović, B. , Jović, N. *et al.* (2013) *Int. J. Appl. Ceram. Technol.*, **10**, 957–969.
[26] Jokanović, V., Čolović, B., Sandić-Živković, M. *et al.* (2016) *Serb. Dental J.,* **63**, 74–84.
[27] Nasiri-Tabrizi, B., Fahami, A., Ebrahimi-Kahrizsangi, R. *et al.* (2013) *Powder Technol.,* **243**, 59–70.
[28] Cullity, B.D (1978) *Elements of X-ray diffraction,* Addison-Wesley Series in Metallurgy and Materials, 2nd edn. Addison Wesley Publishing Company Ltd, Reading, MA.
[29] Capanema, N.S.V., Mansur, A.A.P., Carvalho, S.M., Silva, A.R.P., Ciminelli, V.S. and Mansur, H.S. (2015) *Materials*, **8**, 4191–4209.
[30] Albano, M.P. and Garrido, L.B. (2011) *J. Mater. Sci.,* **46**, 5117–5128.
[31] Freund, F. and Knobel, R.M. (1977) *J. Chem. Soc., Dalton Trans. (1972-1999),* 1136–1140.
[32] Lafon, J.P., Champion, E. and Bernache-Assollant, D. (2008) *J. Eur. Ceram. Soc.,* **28**, 139–147.
[33] Ebrahimi-Kahrizsangi, R., Nasiri-Tabrizi, B. and Chami, A. (2011) *Particuology*, **9**, 537–544.